

# A robust rolling-mode direct-current triboelectric nanogenerator arising from electrostatic breakdown effect

Yikui Gao<sup>a,b,1</sup>, Di Liu<sup>b,c,1</sup>, Linglin Zhou<sup>b,c,1</sup>, Shaoxin Li<sup>b,c</sup>, Zhihao Zhao<sup>b</sup>, Xing Yin<sup>b</sup>, Shengyang Chen<sup>a,b</sup>, Zhong Lin Wang<sup>b,c,d,\*</sup>, Jie Wang<sup>a,b,c,\*</sup>

<sup>a</sup> Center on Nanoenergy Research, School of Physical Science and Technology, Guangxi University, Nanning 530004, PR China

<sup>b</sup> Beijing Institute of Nanoenergy and Nanosystems, Chinese Academy of Sciences, Beijing 101400, PR China

<sup>c</sup> College of Nanoscience and Technology, University of Chinese Academy of Sciences, Beijing 100049, PR China

<sup>d</sup> School of Materials Science and Engineering, Georgia Institute of Technology, Atlanta, GA 30332, USA

## ARTICLE INFO

### Keywords:

Triboelectrification  
Electrostatic breakdown  
Triboelectric nanogenerator  
Rolling mode  
Direct current

## ABSTRACT

With merits of light weight, low cost, and high efficiency even at low frequency, triboelectric nanogenerator (TENG) has been considered as a potential solution for distributed energy for the new era of internet of things (IoTs). However, the conventional TENG always has intrinsic property of high current crest factor, which is unable to drive electronics directly, and its output performance is usually limited by air breakdown and material wear. Here, we designed a rolling-mode direct-current TENG (R-DC-TENG) by coupling triboelectrification effect and electrostatic breakdown for realizing a constant current (crest factor  $\sim 1$ ) output in rolling mode TENG for the first time. The R-DC-TENG shows the output characteristics of a quasi-constant current source, with a stable constant current output at load from 1 k $\Omega$  to 100 M $\Omega$ . More importantly, it exhibits an excellent robustness compared with the reported sliding-mode DC-TENG (S-DC-TENG).

## 1. Introduction

With the rapid development of wearable electronics, internet of things (IoTs) and artificial intelligence, the conventional concentrated power plant is unable to meet the energy demands of the widely distributed sensors around everywhere in a sustainable, renewable, low-cost and self-powered manner [1,2]. From a long-term and environmental perspective, directly harvesting the energy around the environment for the distributed sensors is an ideal choice for the new era [3]. Among the existing energy harvesting methods, mechanical energy harvesting shows its unique advantages of widely distributed, inexhaustible and sustainable characteristics, particularly, closely related to the surrounding environment of distributed sensors [4]. Based on triboelectrification effect and electrostatic induction, triboelectric nanogenerator (TENG), with the characteristics of lightweight, low cost, simplicity in fabrication, and high efficiency especially at low frequency, has been widely studied from fundamental physics to potential applications and demonstrated as a potential solution for distributed energy supply for the new era of IoTs [5–10]. Great efforts have been devoted to

improve the output performance of TENG by material choice, structural design, surface modification, ultrathin dielectric layer and environmental control [3,5,11–14]. Nevertheless, it cannot be used to drive electronic devices directly due to its natural characteristic of alternating current output as well as high current crest factor (The crest factor is defined as the ratio of the peak value to the root-mean square value.) [15–17].

In recent years, the direct-current (DC) generator has gradually attracted people's attention because a constant current is always needed by electronic devices for practical application. Generally, the rectifier is used to convert alternating current to DC output [18–21]. Although electric brushes and air breakdown channel have reported to realize DC output, the current crest factor is still very high and it is not suitable for directly powering electronic devices [16,22,23]. Additionally, based on Schottky knot, silicon p-n junction or contact barrier between metal and semiconductor, a continuous DC output can be realized, but its output voltage cannot be higher than the contact barrier voltage (generally less than 1 V), which is also difficult to directly power most of electronics [24–26]. Very recently, a novel DC-TENG is invented by coupling the

\* Corresponding authors at: Beijing Institute of Nanoenergy and Nanosystems, Chinese Academy of Sciences, Beijing 101400, PR China.

E-mail addresses: [zhong.wang@mse.gatech.edu](mailto:zhong.wang@mse.gatech.edu) (Z.L. Wang), [wangjie@binn.cas.cn](mailto:wangjie@binn.cas.cn) (J. Wang).

<sup>1</sup> These authors contributed equally to this work.

triboelectrification effect with electrostatic breakdown, which is characterized by constant current and high voltage output and demonstrated to drive electronic devices directly [27–32]. However, as a mechanical energy harvesting method by sliding friction, its energy conversion efficiency and robustness may be damaged due to the material wear [33–36]. Therefore, a robust TENG with constant current output is highly desired.

Here, we designed a rolling-mode DC-TENG (R-DC-TENG) based on triboelectrification effect and air breakdown to increase the device durability and achieve a constant current output in the meantime. Firstly, the R-DC-TENG worked on a flat plate confirms that DC output can also be realized at rolling mode friction. Then, the R-DC-TENG was fixed on a rotary motor to realize a continuous output. The R-DC-TENG shows the output characteristics of an approximate constant current source that the output current almost keeps a constant value with the load resistance increasing from 1 k $\Omega$  to 100 M $\Omega$ , and the output charge of the R-DC-TENG can maintain 96% after 90,000 cycles. In addition, its output current has a good linear relationship with the rotation speed, showing a good potential for using as a rotation sensor.

## 2. Working principle of R-DC-TENG

The designed R-DC-TENG mainly comprises a charge collecting electrode (CCE), a rolling frictional electrodes (RFE), and a triboelectric

layer, where an acrylic tube was used to maintain the R-DC-TENG balance (Fig. 1a), of course, which can be used as another rolling frictional electrode. Here, the copper foil was used as the RFE, the polytetrafluoroethylene (PTFE) film as the triboelectric layer, and a stainless steel blade as the CCE. The surface of PTFE film was etched to nanostructure to enhance both triboelectrification and air breakdown. To further enhance the process of air breakdown, the gap distance between PTFE film and the CCE (Fig. 1a) is controlled by adjusting the screw pitch inside on the structure of CCE to get close or get away from the PTFE film. The detailed working mechanism of R-DC-TENG is illustrated in Fig. 1b. In the initial state (Fig. 1b (i)), when the rolling structure contacts with the surface of PTFE film, the RFE will be positively charged and the PTFE film will be negatively charged due to contact electrification. The negative charges on the surface of PTFE film can exist for a long time because the PTFE film is an electret. In the medium state (Fig. 1b (ii)), the rolling structure keeps rolling on the surface of PTFE film under an external force, and thus a very high electrostatic field will build across the gap between the CCE and PTFE film. When the electric field strength exceeds the critical breakdown field strength of air dielectric (according to Paschen's law) [37], the air in the gap distance will be ionized and become conductive, and electrons will then transfer from the surface of PTFE to the CCE. If the rolling structure continuous to move forward, a continuous DC output will flow in external circuit until the rolling structure reaching the right end of the PTFE film.

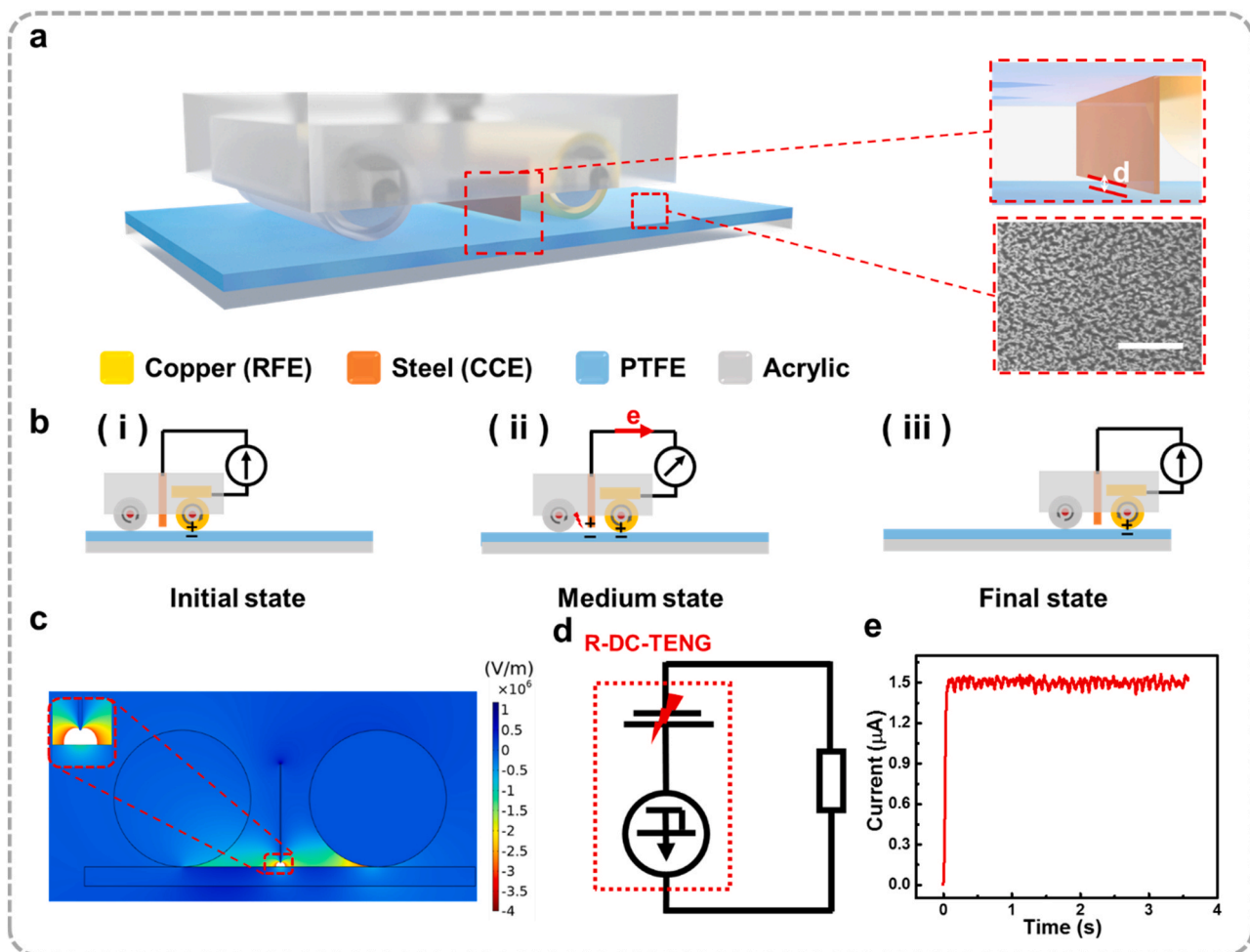


**Fig. 1.** Structural design and working principle of the R-DC-TENG. (a) Schematic illustration of the R-DC-TENG. The zoomed-in illustration demonstrates the gap between CCE and PTFE and scanning electron microscopy (SEM) image of the PTFE surface (Scale bar, 10  $\mu\text{m}$ ). (b) The working mechanism of R-DC-TENG. (c) The COMSOL simulation result of electrostatic field intensity between the CCE and PTFE film at the short-circuit condition. The zoomed-in illustration demonstrates the electrostatic field intensity near the tip. The electric field intensity in the blank area exceeds 3  $\text{MV m}^{-1}$ . (d) Equivalent circuit model of the R-DC-TENG. (e) Constant current output of the R-DC-TENG.

Because the direction of the electric field is unidirectional, the output current will also be in a single direction [31]. In the final state (Fig. 1b (iii)), when the rolling structure moves backward from the right end to the left end, there will be no current flow in external circuit, because the negative charge mainly distributed on the PTFE film of the RFEs right side due to contact electrification, there are not enough electrostatic charges on the surface of PTFE film below the CCE, the electric field strength of the gap is not enough for air breakdown. In a word, if the rolling structure keeps rolling before the CCE, and the electrostatic charges on the surface of PTFE film are enough for air breakdown, and then a DC output will always flow in external circuit. The theoretical simulation result by COMSOL Multiphysics also confirms the breakdown effect in our R-DC-TENG, because the highest electric field always exists at the gap between CCE and PTFE making it prone to air breakdown, as shown in Fig. 1c.

From a circuit perspective, the air gap between the CCE and PTFE film can be represented by a broken-down capacitor ( $C_0$ ), and the process of rolling electrification between the RFEs and the PTFE film can be considered as a charge source ( $Q_0$ ), which is shown in Figs. 1d and S1. The charge source creates charges that are stored in the air dielectric capacitor. A strong electric field will be built between the air gap and gradually increase until the capacitor breakdown, and then a DC output can be obtained. Note that the air dielectric capacitor is very small, if

enough charges could maintain the potential difference of the capacitor, due to the capacitor delay effect, a constant current is finally realized by using the rotary R-DC-TENG in  $600 \text{ r min}^{-1}$  (Fig. 1e).

### 3. Results and discussion

#### 3.1. DC output in R-DC-TENG

We firstly investigated the effect of RFE number on the performance of R-DC-TENG, as shown in Fig. S2. When there is only one RFE, both of the transferred charges and the output current are relatively low and unstable. With the number of RFEs increasing from two to four, the transferred charges increase gradually, and the output current is gradually stable, which might result from the enhanced triboelectric charges by increasing the number of RFE. Considering the stability of output performance and size optimization of the R-DC-TENG, we choose four RFEs to carry out the following experiment. Next, we tested several common materials (Fluorinated ethylene propylene (FEP), Polyimide (PI), Poly-ether-ether-ketone (PEEK) and PTFE) on output performance (Fig. S3). The results indicate that FEP and PTFE have similar output performance, and PEEK and PI are poorer than FEP and PTFE on output performance. Given that PTFE has better wear resistance and smaller friction coefficient, PTFE is chosen as the triboelectric material in the

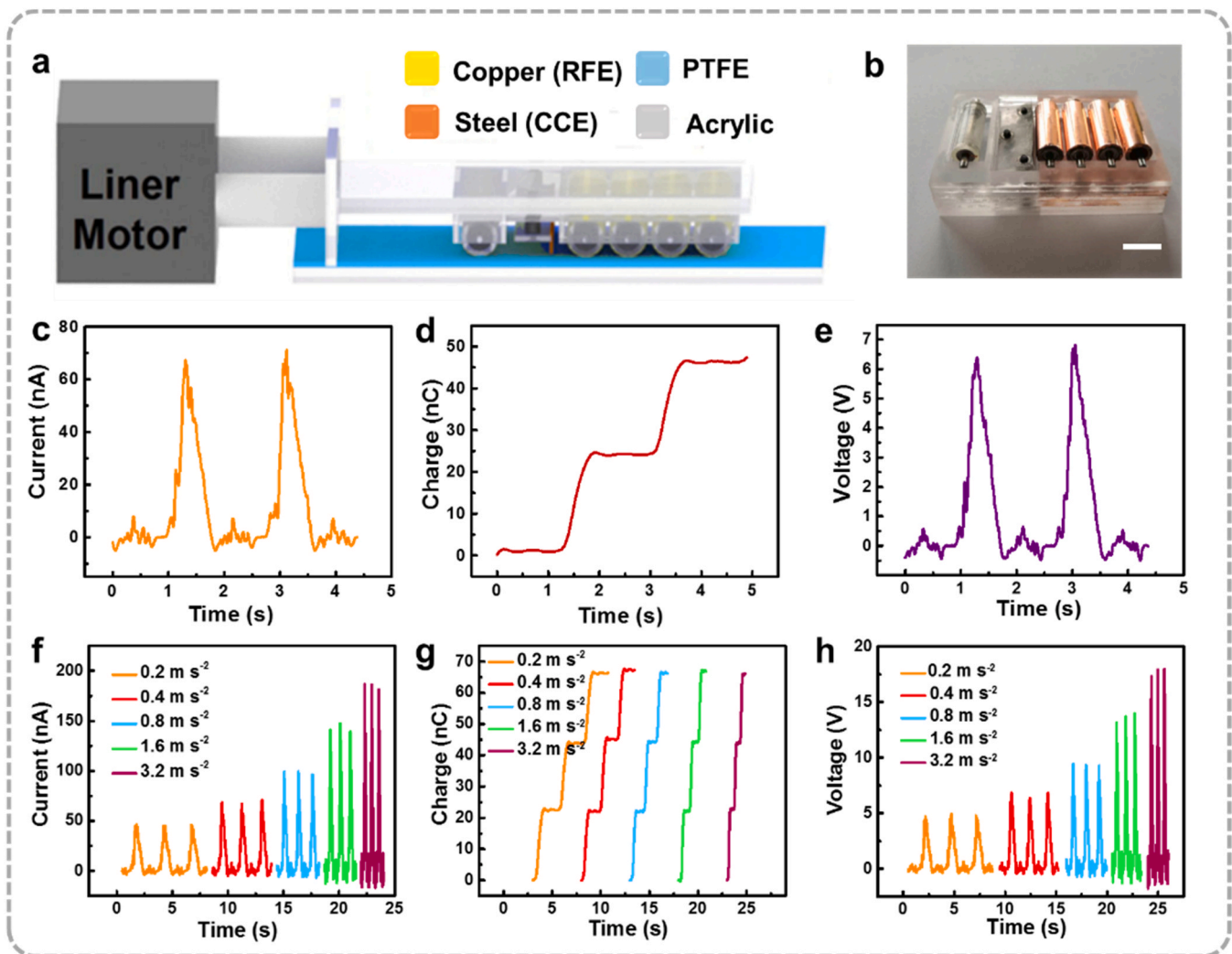


Fig. 2. Output performance of the R-DC-TENG. (a) Working state of the R-DC-TENG. (b) The photograph of the R-DC-TENG (Scale bar, 1 cm). (c) Short-circuit current, (d) transferred charges and (e) output voltage of the R-DC-TENG. (f) Short-circuit current, (g) transferred charges and (h) output voltage of the R-DC-TENG at various accelerations.

experiment. The output performance of the single R-DC-TENG was studied by using a programmable linear motor where the PTFE surface was pre-cleaned by deionized water and alcohol to remove the residual charges (Fig. 2a and b). All of the output current, transferred charges and output voltage have DC output characteristics (Fig. 2c–e), when the linear motor is in a reciprocating linear motion with a constant acceleration. During one cycle, electrons transfer in external circuit only when the rolling structure moves forward, and there are nearly no electrons being transferred when the rolling structure moves backward, which is in accordance with the working mechanism of the R-DC-TENG. With the increasing of acceleration from  $0.2 \text{ m s}^{-2}$  to  $3.2 \text{ m s}^{-2}$ , the output current increases from  $46.2 \text{ nA}$  to  $186.5 \text{ nA}$ , and the output voltage also increases from  $4.8 \text{ V}$  to  $17.9 \text{ V}$  as shown in Fig. 2f and h, and the testing method of the output voltage is displayed in Fig. S4. Note that the transferred charges always maintain a constant value at different accelerations (Fig. 2g), because it only depends on the area of the charged region that the CCE sweeps, which remains unchanged at various accelerations in this test environment. We also tested the output performance of the device at various speeds, and the output current increases with speed from  $20.9 \text{ nA}$  at  $0.05 \text{ m s}^{-1}$  to  $81.5 \text{ nA}$  at  $0.20 \text{ m s}^{-1}$ , and the output voltage increases from  $2.1 \text{ V}$  at  $0.05 \text{ m s}^{-1}$  to  $7.8 \text{ V}$  at  $0.20 \text{ m s}^{-1}$  as well (Fig. S5a and S5c). As shown in Fig. S5b, the amount of charge transferred in external circuit is about  $21 \text{ nC}$  during each cycle, and there is a good linear relationship between current and speed (Fig. S5d and Note S1). As shown in Note S2 and Fig. S6, improving the triboelectrification by increasing the number of RFE, the R-DC-TENG has a constant current output trend under the condition of uniform motion.

### 3.2. Rotary R-DC-TENG

To obtain a constant current output, we replace the reciprocating motion on a flat plate by a rotary motion, where the R-DC-TENG can rotate around an axis, and it is more suitable for collecting mechanical energy around environment (such as wind and water energy) for practical application [35]. More importantly, the steady mechanical rotational motion is better for realizing a stable output. The specific structure of this device is shown in Fig. 3a, which is composed of six CCEs, six RFEs, a rotor, and two fixing plates which have holes for fixing RFEs and CCEs. Rotor is the PTFE film wrapped in the acrylic tube with soft sponge foam between them. The soft sponge foam acts as a buffer layer to assure intimate contact between the PTFE film and RFEs. There is a gap distance between CCE and PTFE films as shown in the partial enlarged drawing of Fig. 3b, which can be adjusted by the screws on the CCE to better optimize the R-DC-TENG output, and the detailed structure of CCE is shown in Fig. 3c and d. The mechanism of the rotary R-DC-TENG is similar to that of reciprocating motion of R-DC-TENG (Fig. 3e).

Here, the amount of CCEs are investigated to optimize the output performance of R-DC-TENG. Keeping the number of RFEs as six, the quantity ratio of CCEs and RFEs was set as 1:6, 1:3, 1:2, and 1:1 by increasing the number of CCEs (Fig. 4a). According to the different quantity ratio, the equivalent circuit diagram of the device can be regarded as multiple R-DC-TENGs in parallel (named  $m$ ,  $m = 1, 2, 3$  and  $6$ ) (Fig. 4b). According to Fig. 4c and d, it takes  $3.0 \text{ s}$ ,  $1.7 \text{ s}$ ,  $1.5 \text{ s}$  and  $1.4 \text{ s}$  for the device to collect  $2 \mu\text{C}$  charges for R-DC-TENG with the quantity ratio of 1:6, 1:3, 1:2, and 1:1 at  $600 \text{ r min}^{-1}$ , respectively. The corresponding short-circuit current of the device are  $0.66 \mu\text{A}$ ,  $1.20 \mu\text{A}$ ,

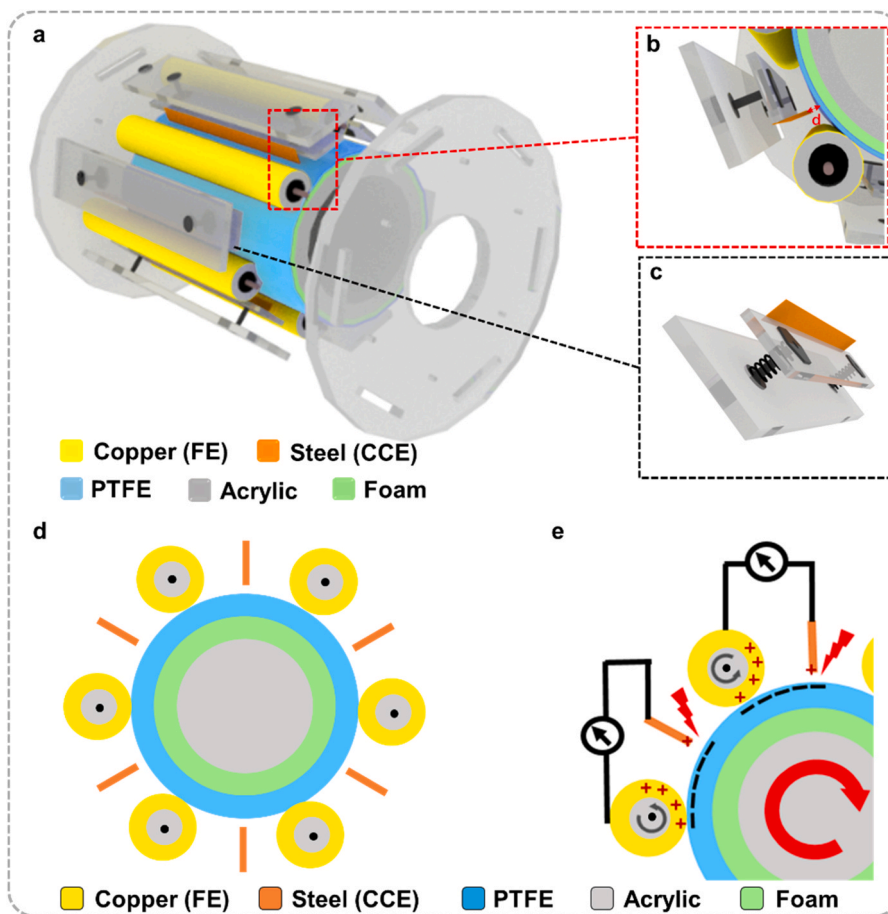


**Fig. 3.** Structural design and working principle of the rotary R-DC-TENG. (a) Schematic illustration of the rotary R-DC-TENG. (b) The gap between CCE and PTFE. (c) The structure of CCE. (d) The physical model and (e) working mechanism of the rotary R-DC-TENG.

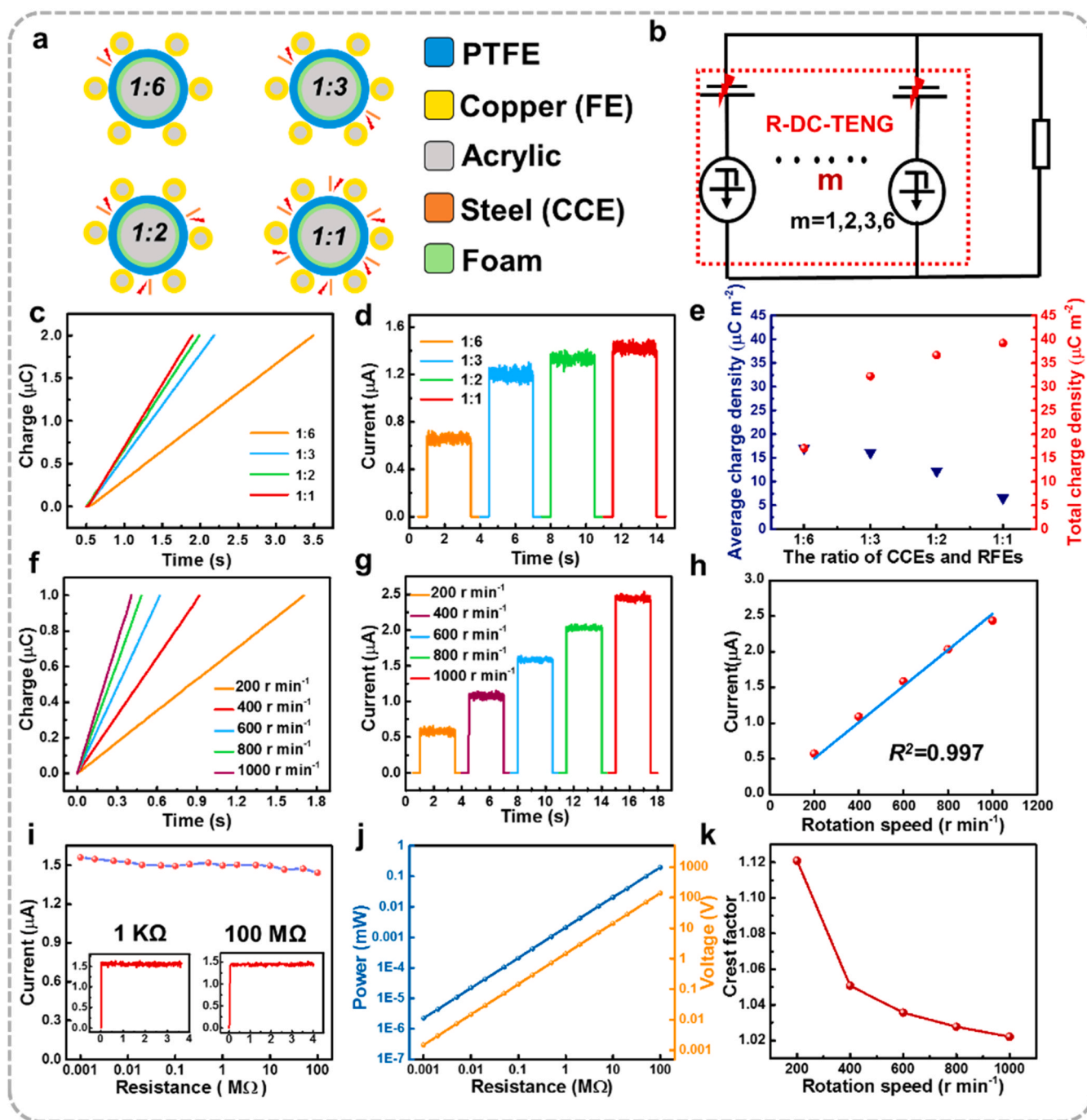


**Fig. 4.** Output performance of the rotary R-DC-TENG. (a) Four physical model of the rotary R-DC-TENG with different number of CCEs. (b) Equivalent circuit model of the rotary R-DC-TENG in different working modes. (c) Transferred charges and (d) short-circuit current of the rotary R-DC-TENG in four working modes. (e) The total transferred charge density of the rotary R-DC-TENG and the transferred charge density on single CCE. (f) Transferred charges and (g) short-circuit current of the rotary R-DC-TENG at different rotation rates. (h) The linear relationship between  $I_{SC}$  and rotation speed. (i) Output current of the rotary R-DC-TENG with various resistances. Insets show the detailed output current at 1 k $\Omega$  and 100 M $\Omega$  resistances. (j) Output voltage and output power of the rotary R-DC-TENG with various resistances. (k) Crest factor of output current of R-DC-TENG at different rotation speed.

1.35  $\mu\text{A}$  and 1.43  $\mu\text{A}$ . Fig. 4e shows the total transferred charge density of the rotary R-DC-TENG and the average transferred charge density of single CCE under different quantity ratios, and when the quantity ratio of CCEs and RFEs is 1:6, we can observe that the total transferred charge density and the average transferred charge density of R-DC-TENG are both  $17.05 \mu\text{C m}^{-2}$ . With the quantity ratio increasing, the total transferred charge density of R-DC-TENG improves, while the average transferred charge density of single CCE declines. The maximum total transferred charge density of  $39.20 \mu\text{C m}^{-2}$  is achieved when the

quantity ratio is 1:1. In other words, with a certain number of RFEs, the total performance of R-DC-TENG gradually increases to the maximum with the increasing of the number of CCEs (Fig. S7 and Note S3). This also means that the output of R-DC-TENG can be further improved through the reasonably designing of spatial structure. Based on the above research, the device with quantity ratio of 1:1 was used to complete the following experiments.

According to previous studies, the short-circuit current ( $I_{SC}$ ) can be explained by the following formula:

$$I_{SC} = \frac{dQ_{AB}}{dt} = \frac{RL\sigma_{AB}d\theta}{d\theta/\omega} = RL\sigma_{AB}\omega \quad (1)$$

where  $\sigma_{AB}$  is the transferred charge density due to air breakdown,  $R$  is the radius of rotor,  $L$  is the length of the single CCE,  $\theta$  is the rotation angular of rotor and  $\omega$  is the angular velocity. From the above equation, we can know that the output current has a linear relationship with the rotation speed. Fig. 4f and g show the consumed time of collecting 2  $\mu\text{C}$  charges and the output current at various rotation speeds. With rotation speed increasing from 200  $\text{r min}^{-1}$  to 1000  $\text{r min}^{-1}$ , the output current increases from 0.57  $\mu\text{A}$  to 2.48  $\mu\text{A}$ , respectively. According to the formula of  $I_{SC}$ , we find that it is proportional to the angular velocity of the device. As displayed in Fig. 4h,  $I_{SC}$  has a good linear relationship with rotation speed ( $R^2 = 0.997$ ), showing great potential of our designed R-DC-TENG for wind speed sensor. Moreover, various load resistances ranging from 1  $\text{k}\Omega$  to 100  $\text{M}\Omega$  were utilized as the external load to further investigate the performance of the R-DC-TENG at 600  $\text{r min}^{-1}$ . We notice that the current only decreases slightly (from 1.56  $\mu\text{A}$  to 1.44  $\mu\text{A}$ ) as the external resistance increasing from 1  $\text{k}\Omega$  to 100  $\text{M}\Omega$  (Fig. 4i). Besides, the corresponding output voltage and power also increase from 1.5 mV to 140 V and from 2.25 nW to 0.2 mW, respectively (Fig. 4j). All of these results indicate that the rotary R-DC-TENG has the characteristics of the constant current source. As shown in Fig. 4k, the crest factor of the output current signal at various rotating speeds is close to 1 (1.12 at 200  $\text{r min}^{-1}$  and 1.02 at 1000  $\text{r min}^{-1}$ ), and the formula of crest factor ( $K$ ) of the output current is shown as follow:

$$K = \frac{I_{max}}{\sqrt{\int P dt}/t} \quad (2)$$

These mean that the R-DC-TENG can drive the electronic device very stably when the output current is sufficient, and it is a particular output

characteristic of DC-TENG.

### 3.3. Applications of R-DC-TENG

To demonstrate the constant current output characteristics and the enlarged device durability of our designed R-DC-TENG for practical applications, the electronic devices are directly connected with the R-DC-TENG without any rectifier even energy storage unit. The equivalent circuit diagram of the test system is shown in Fig. 5a. When the switch is on, the R-DC-TENG can power the load directly with a voltage meter for measuring the output voltage simultaneously. Fig. 5b shows the voltage curves of a capacitor with a capacitance of 1.1  $\mu\text{F}$  charged directly by the rotary R-DC-TENG without a rectifier at various rotation speeds (200, 400, 600, 800 and 1000  $\text{r min}^{-1}$ ). The charging rate increases with the rotation speed, and the capacitor can be charged to 10 V within 5 s at 1000  $\text{r min}^{-1}$ . Fig. 5c depicts the charging curves of different capacitors (1.1, 2.2, and 4.4  $\mu\text{F}$ ) charged by the rotary R-DC-TENG at 600  $\text{r min}^{-1}$ . The linear increase of the voltage curves in response time suggests a continuous and stable output performance of R-DC-TENG.

An LED light bulb array (40 bulbs in series) can also be lit by the rotary R-DC-TENG working at 600  $\text{r min}^{-1}$ . Unlike LEDs driven by the conventional TENG with alternating current output, these LEDs powering by the constant current output remain at constant luminance without flashing lights, which is the best representation of its constant current output characteristics (Fig. 5d and Movie S1). We also examined the stability of R-DC-TENG by long-term continuous rotation and the results are shown in Fig. 5e, the output charge of the R-DC-TENG can maintain 96% after 90,000 cycles, however, the output charge of the sliding-mode DC-TENG (S-DC-TENG) only maintain 48% after 90,000 cycles, which proves that the replacement of sliding movement by the rotary motion is an excellent method for improving the stability of DC-

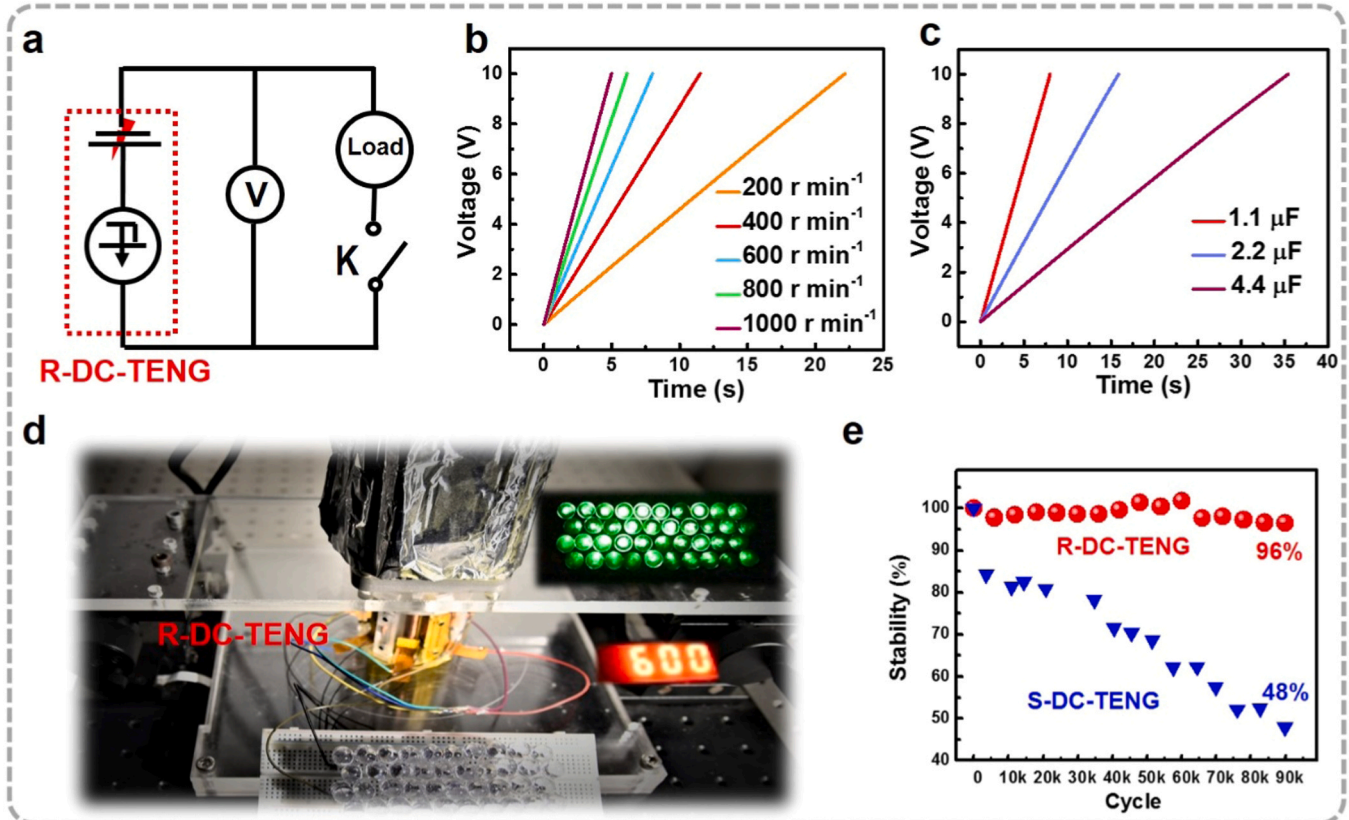


Fig. 5. Applications of the rotary R-DC-TENG. (a) Circuit diagram of the rotary R-DC-TENG for charging a capacitor. (b) Charging curves of different capacitors charged by the rotary R-DC-TENG at 600  $\text{r min}^{-1}$ . (c) Measured voltages of various capacitors charged by the rotary R-DC-TENG at a rotating speed of 600  $\text{r min}^{-1}$ . (d) The rotary R-DC-TENG drives small bulb-arrays at 600  $\text{r min}^{-1}$ . (e) The comparison of output stability between the rotary R-DC-TENG and sliding DC-TENG.

TENG. The structure of S-DC-TENG is shown in Fig. S8.

Supplementary material related to this article can be found online at [doi:10.1016/j.nanoen.2021.106014](https://doi.org/10.1016/j.nanoen.2021.106014).

#### 4. Conclusion

In summary, we designed a R-DC-TENG based on triboelectrification effect and air breakdown, and a constant current output is realized in the rolling-mode electrification for the first time. The R-DC-TENG was firstly placed on a flat plate to confirm that a DC output can be realized by using rolling friction. Then a rotary R-DC-TENG was designed to achieve a constant current output. By investigating the quantity ratio of CCEs and RFEs, we found that the surface charge density can be increased by multiple cycles of rolling friction. By optimizing the quantity ratio of CCEs and RFEs, a greatest constant current output was achieved with a quantity ratio of 1:1. Additionally, the constant current output of R-DC-TENG has also been demonstrated to power electronics without any rectifier and energy storage unit. Moreover, the stability of DC-TENG has been greatly improved by replacing sliding motion to the rolling motion. This work provide a promising methodology to prolong the lifetime of DC-TENG, and we also provide a reliable way (fixed the amount of RFEs and control the amount of CCEs) to improve its output performance through reasonable structure design, and the output current of R-DC-TENG has a good linear relationship with the rotation speed which shows good potential for rotation sensor.

#### 5. Experimental methods

##### 5.1. Fabrication of the RFE

One acrylic tube (outer diameter, 7 mm; inner diameter, 5 mm; length, 20 mm) was wrapped with copper tape, and then bearings (MR52) were inserted at the two ends of the acrylic tube, and finally the steel rods with length of 30 mm and diameter of 2 mm were finally passed through the bearings. This is used for the fabrication of the linear-motion R-DC-TENG. The other acrylic tube (outer diameter, 7 mm; inner diameter, 5 mm; length, 40 mm) was wrapped with copper tape, and then bearings (MR52) were inserted at the two ends of the acrylic tube, and finally the steel bars with length of 50 mm and diameter of 2 mm were finally passed through the bearings. This is used for the fabrication of the rotary R-DC-TENG.

##### 5.2. Fabrication of the CCE

One acrylic sheet (length, 30 mm; width, 7 mm) was cut as the substrate using a laser cutter with two hexagonal holes in the middle of the acrylic plate to hold the nut, and the blade with length of 30 mm and width of 5 mm was attached to one side of the acrylic sheet, which is used for the fabrication of the linear-motion R-DC-TENG. The other acrylic sheet (length, 40 mm; width, 7 mm) was cut as the substrate using a laser cutter with two hexagonal holes in the middle of the acrylic plate to hold the nut, and the blade with length of 37 mm and width of 5 mm was attached to one side of the acrylic sheet, which is used for the fabrication of the rotary R-DC-TENG.

##### 5.3. Fabrication of the linear-motion R-DC-TENG

Four rectangular acrylic plates were cut as the substrate using a laser cutter, and the four plates are numbered 1, 2, 3, 4 from top to bottom. Plate 2, 3, 4 (outer length, 60 mm; outer width, 40 mm; thickness, 2 mm) were cut three rectangular spaces for placing CCEs (inner length, 10 mm; inner width, 30 mm), RFEs (inner length, 32 mm; inner width, 26 mm) and acrylic tubes (inner length, 8 mm; inner width, 26 mm). Plate 4 has ten square holes, which was used to fix steel bars, and two holes (diameter, 2 mm) were left in plate 1 to hold the screws, which were used to fix CCE. A layer of foam (length, 30 mm; width, 10 mm;

thickness, 1 mm) was fixed on the back of plate 1, and copper plates were attached on the surface of the foam to form a brush. Finally, acrylic glue was used to fix each part of the R-DC-TENG. PTFE with thickness of 0.05 mm was used as a triboelectric layer, and there was a layer of foam (200 mm × 60 mm × 1 mm) between the acrylic plate (200 mm × 60 mm × 3 mm) and PTFE to achieve soft contact.

##### 5.4. Fabrication of the rotary R-DC-TENG

Six acrylic sheets (55 mm × 10 mm × 3 mm) with two round holes (diameter, 2 mm) were cut by a laser cutter, and screws and springs were used to connect the CCE and them. Cut two acrylic round plates (diameter, 60 mm; thickness, 3 mm) with circular holes (diameter, 36 mm) in the middle, six small round holes (diameter, 2 mm) and six small square holes (length, 10 mm; width, 3 mm) were distributed equably around the circle hole, their positions from the center of the circle are 20 mm and 27 mm, respectively. Fix the RFEs and CCEs on the acrylic round plates. The PTFE film with the thickness of 0.05 mm was used as a triboelectric layer, and there was a layer of foam (94.2 mm × 40 mm × 1 mm) between the acrylic tube (length, 40 mm; diameter, 30 mm) and the PTFE layer to achieve soft contact.

##### 5.5. Method of controlling the gap

In this experiment, we control the gap between the dielectric layer and CCE by turning the screw, where the pitch of the screw is 0.4 mm, which means that CCE can move up 0.4 mm by turning the screw 360°. We can control the gap of the rotary R-DC-TENG by turning the screw about 180° with a cross screwdriver and the CCE can be moved up 0.2 mm, when the CCE contacts with the dielectric layer. We can control the gap of the linear-motion R-DC-TENG by turning the screw about 45° with a cross screwdriver and the CCE can be moved up 0.05 mm, when the CCE contacts with the dielectric layer.

##### 5.6. COMSOL simulation

The electrostatic field between the CCE and PTFE film was calculated using the commercial software COMSOL. Relative permittivity of the PTFE was set as 2.5, and relative permittivity of the PMMA was set as 3.4. The distance between the CCE and PTFE layer was set as 0.2 mm. The surface charge density of the PTFE film was  $17 \mu\text{C m}^{-2}$ . The total surface charges of PTFE film are equal to the charges in electrodes but opposite in polarity. The CCEs and RFEs were set at the same potential.

##### 5.7. Electrical measurement and characterization

A programmable electrometer (Keithley Instruments model 6514) was adopted to measure the short-circuit current, transferred charges and current signal at the load of 100 MΩ. The linear process was conducted by a linear motor (TSMV120-1S). The rotary process was operated by a rotational motor (80BL165S75-3130TKO). The capacitance and voltage of capacitor were monitored by a potentiostat (Bio-Logic VSP-300, France). The SEM image of the surface of PTFE was taken with a Hitachi field emission scanning electron microscopy (SU 8020).

#### CRediT authorship contribution statement

**Gao Yikui:** Conceptualization, Investigation, Writing - original draft. **Liu Di:** Conceptualization, Investigation, Writing - original draft. **Zhou Linglin:** Conceptualization, Investigation, Writing - original draft. **Li Shaoxin:** Experiment. Experiment. **Zhao Zhihao:** Experiment. **Yin Xing:** **Chen Shengyang:** Experiment. **Wang Zhong Lin:** Supervision, Writing - review & editing. **Wang Jie:** Supervision, Conceptualization, Writing - review & editing.

## Declaration of Competing Interest

The authors declare that they have no known competing financial interests or personal relationships that could have appeared to influence the work reported in this paper.

## Acknowledgements

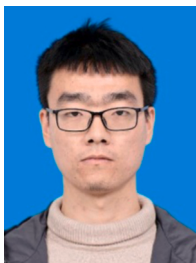
Research was supported by the National Key Research and Development Project from Ministry of Science and Technology (2016YFA0202701), National Natural Science Foundation of China (Grant No. 61774016, 5151101243, 51561145021), Beijing Municipal Science & Technology Commission (Z171100000317001, Z171100002017017, Y3993113DF). Patents have been filed based on the research results presented in this manuscript. Y. Gao, D. Liu and L. Zhou contributed equally to this work.

## Appendix A. Supporting information

Supplementary data associated with this article can be found in the online version at [doi:10.1016/j.nanoen.2021.106014](https://doi.org/10.1016/j.nanoen.2021.106014).

## References

- Z.L. Wang, Entropy theory of distributed energy for internet of things, *Nano Energy* 58 (2019) 669–672, <https://doi.org/10.1016/j.nanoen.2019.02.012>.
- S. Chu, A. Majumdar, Opportunities and challenges for a sustainable energy future, *Nature* 488 (2012) 294–303, <https://doi.org/10.1038/nature11475>.
- J. Wang, C.S. Wu, Y.J. Dai, Z.H. Zhao, A. Wang, T.J. Zhang, Z.L. Wang, Achieving ultrahigh triboelectric charge density for efficient energy harvesting, *Nat. Commun.* 8 (2017) 88, <https://doi.org/10.1038/s41467-017-00131-4>.
- Z.L. Wang, Triboelectric nanogenerator (TENG)—sparking an energy and sensor revolution, *Adv. Energy Mater.* 10 (2020), 2000137, <https://doi.org/10.1002/aenm.202000137>.
- C.L. Zhang, L.L. Zhou, P. Cheng, X. Yin, D. Liu, X.Y. Li, H.Y. Guo, Z.L. Wang, J. Wang, Surface charge density of triboelectric nanogenerators: theoretical boundary and optimization methodology, *Appl. Mater. Today* 18 (2020), 100496, <https://doi.org/10.1016/j.apmt.2019.100496>.
- J.J. Shao, M. Willatzen, Y.J. Shi, Z.L. Wang, 3D mathematical model of contact-separation and single-electrode mode triboelectric nanogenerators, *Nano Energy* 60 (2019) 630–640, <https://doi.org/10.1016/j.nanoen.2019.03.072>.
- J. Chung, D. Heo, G. Shin, D. Choi, K. Choi, D. Kim, S. Lee, Ion-enhanced field emission triboelectric nanogenerator, *Adv. Energy Mater.* 9 (2019), 1901731, <https://doi.org/10.1002/aenm.201901731>.
- G.L. Liu, L.F. Xiao, C.Y. Chen, W.L. Liu, X.J. Pu, Z.Y. Wu, C.G. Hu, Z.L. Wang, Power cables for triboelectric nanogenerator networks for large-scale blue energy harvesting, *Nano Energy* 75 (2020), 104975, <https://doi.org/10.1016/j.nanoen.2020.104975>.
- Z.M. Lin, B.B. Zhang, H.Y. Guo, Z.Y. Wu, H.Y. Zou, J. Yang, Z.L. Wang, Super-robust and frequency-multiplied triboelectric nanogenerator for efficient harvesting water and wind energy, *Nano Energy* 64 (2019), 103908, <https://doi.org/10.1016/j.nanoen.2019.103908>.
- G.L. Liu, J. Chen, Q. Tang, L. Feng, H.M. Yang, J.E. Li, Y. Xi, X. Wang, C.G. Hu, Wireless electric energy transmission through various isolated solid media based on triboelectric nanogenerator, *Adv. Energy Mater.* 8 (2018), 1703086, <https://doi.org/10.1002/aenm.201703086>.
- W.L. Liu, Z. Wang, G. Wang, G.L. Liu, J. Chen, X.J. Pu, Y. Xi, X. Wang, H.Y. Guo, C. G. Hu, Z.L. Wang, Integrated charge excitation triboelectric nanogenerator, *Nat. Commun.* 10 (2019) 1426, <https://doi.org/10.1038/s41467-019-09464-8>.
- H.Y. Zou, Y. Zhang, L.T. Guo, P.H. Wang, X. He, G.Z. Dai, H.W. Zheng, C.Y. Chen, A.C. Wang, C. Xu, Z.L. Wang, Quantifying the triboelectric series, *Nat. Commun.* 10 (2019) 1427, <https://doi.org/10.1038/s41467-019-09461-x>.
- Y.L. Zi, S.M. Niu, J. Wang, Z. Wen, W. Tang, Z.L. Wang, Standards and figure-of-merits for quantifying the performance of triboelectric nanogenerators, *Nat. Commun.* 6 (2015) 8376, <https://doi.org/10.1038/ncomms9376>.
- S.H. Wang, Y.L. Zi, Y.S. Zhou, S.M. Li, F.R. Fan, L. Lin, Z.L. Wang, Molecular surface functionalization to enhance the power output of triboelectric nanogenerators, *J. Mater. Chem. A* 4 (2016) 3728–3734, <https://doi.org/10.1039/C5TA10239A>.
- H. Ryu, J.H. Lee, U. Khan, S.S. Kwak, R. Hinchet, S.W. Kim, Sustainable direct current powering a triboelectric nanogenerator via a novel asymmetrical design, *Energy Environ. Sci.* 11 (2018) 2057–2063, <https://doi.org/10.1039/C8EE00188J>.
- C.Y. Chen, H.Y. Guo, L.J. Chen, Y.C. Wang, X.J. Pu, W.D. Yu, F.M. Wang, Z.Q. Du, Z.L. Wang, Direct current fabric triboelectric nanogenerator for biomotion energy harvesting, *ACS Nano* 14 (2020) 4585–4594, <https://doi.org/10.1021/acsnano.0c00138>.
- X.Y. Li, X. Yin, Z.H. Zhao, L.L. Zhou, D. Liu, C.L. Zhang, C.G. Zhang, W. Zhang, S. X. Li, J. Wang, Z.L. Wang, Long-lifetime triboelectric nanogenerator operated in conjunction modes and low crest factor, *Adv. Energy Mater.* 10 (2020), 1903024, <https://doi.org/10.1002/aenm.201903024>.
- F.B. Xi, Y.K. Pang, W. Li, T. Jiang, L.M. Zhang, T. Guo, G.X. Liu, C. Zhang, Z. L. Wang, Universal power management strategy for triboelectric nanogenerator, *Nano Energy* 37 (2017) 168–176, <https://doi.org/10.1016/j.nanoen.2017.05.027>.
- S.X. Xu, L. Zhang, W.B. Ding, H.Y. Guo, X.H. Wang, Z.L. Wang, Self-doubled-rectification of triboelectric nanogenerator, *Nano Energy* 66 (2019), 104165, <https://doi.org/10.1016/j.nanoen.2019.104165>.
- Z. Wang, W.L. Liu, W.C. He, H.Y. Guo, L. Long, Y. Xi, X. Wang, A.P. Liu, C.G. Hu, Ultrahigh electricity generation from low-frequency mechanical energy by efficient energy management, *Joule* 5 (2021) 441–455, <https://doi.org/10.1016/j.joule.2020.12.023>.
- W.L. Liu, Z. Wang, G. Wang, Q.X. Zeng, W.C. He, L.Y. Liu, X. Wang, Y. Xi, H.Y. Guo, C.G. Hu, Z.L. Wang, Switched-capacitor-convertors based on fractal design for output power management of triboelectric nanogenerator, *Nat. Commun.* 11 (2020) 1883, <https://doi.org/10.1038/s41467-020-15373-y>.
- C. Zhang, T. Zhou, W. Tang, C.B. Han, L.M. Zhang, Z.L. Wang, Rotating-disk-based direct-current triboelectric nanogenerator, *Adv. Energy Mater.* 4 (2014), 1301798, <https://doi.org/10.1002/aenm.201301798>.
- D. Liu, L.L. Zhou, Z.L. Wang, J. Wang, Triboelectric nanogenerator: from alternating current to direct current, *iScience* 24 (2021), 102018, <https://doi.org/10.1016/j.isci.2020.102018>.
- J. Liu, A. Goswami, K. Jiang, F. Khan, S. Kim, R. McGee, Z. Li, Z. Hu, J. Lee, T. Thundat, Direct-current triboelectricity generation by a sliding Schottky nanoncontact on MoS<sub>2</sub> multilayers, *Nat. Nanotechnol.* 13 (2018) 112–116, <https://doi.org/10.1038/s41565-017-0019-5>.
- S.S. Lin, Y.H. Lu, S.R. Feng, Z.Z. Hao, Y.F. Yan, A high current density direct-current generator based on a moving van der Waals Schottky diode, *Adv. Mater.* 31 (2019), 1804398, <https://doi.org/10.1002/adma.201804398>.
- R. Xu, Q. Zhang, J. Wang, D. Liu, J.Y. Wang, Z.L. Wang, Direct current triboelectric cell by sliding an n-type semiconductor on a p-type semiconductor, *Nano Energy* 66 (2019), 104185, <https://doi.org/10.1016/j.nanoen.2019.104185>.
- D. Liu, L.L. Zhou, S.X. Li, Z.H. Zhao, X. Yin, Z.Y. Yi, C.L. Zhang, X.Y. Li, J. Wang, Z. L. Wang, Hugely enhanced output power of direct-current triboelectric nanogenerators by using electrostatic breakdown effect, *Adv. Mater. Technol.* 5 (2020), 2000289, <https://doi.org/10.1002/admt.202000289>.
- S.X. Li, D. Liu, Z.H. Zhao, L.L. Zhou, X. Yin, X.Y. Li, Y.K. Gao, C.G. Zhang, Q. Zhang, J. Wang, Z.L. Wang, A fully self-powered vibration monitoring system driven by dual-mode triboelectric nanogenerators, *ACS Nano* 14 (2020) 2475–2482, <https://doi.org/10.1021/acsnano.9b10142>.
- L.L. Zhou, D. Liu, S.X. Li, Z.H. Zhao, C.L. Zhang, X. Yin, L. Liu, S.N. Cui, Z.L. Wang, J. Wang, Rationally designed dual-mode triboelectric nanogenerator for harvesting mechanical energy by both electrostatic induction and dielectric breakdown effects, *Adv. Energy Mater.* 10 (2020), 2000965, <https://doi.org/10.1002/aenm.202000965>.
- L.L. Zhou, D. Liu, Z.H. Zhao, S.X. Li, Y.B. Liu, L. Liu, Y.K. Gao, Z.L. Wang, J. Wang, Simultaneously enhancing power density and durability of sliding-mode triboelectric nanogenerator via interface liquid lubrication, *Adv. Energy Mater.* 10 (2020), 2002920, <https://doi.org/10.1002/aenm.202002920>.
- D. Liu, X. Yin, H.Y. Guo, L.L. Zhou, X.Y. Li, C.L. Zhang, J. Wang, Z.L. Wang, A constant current triboelectric nanogenerator arising from electrostatic breakdown, *Sci. Adv.* 5 (2019), eaav6437, <https://doi.org/10.1126/sciadv.aav6437>.
- Z.H. Zhao, Y.J. Dai, D. Liu, L.L. Zhou, S.X. Li, Z.L. Wang, J. Wang, Rationally patterned electrode of direct-current triboelectric nanogenerators for ultrahigh effective surface charge density, *Nat. Commun.* 11 (2020) 6186, <https://doi.org/10.1038/s41467-020-20045-y>.
- P. Bai, G. Zhu, Y. Liu, J. Chen, Q.S. Jing, W.Q. Yang, J.S. Ma, G. Zhang, Z.L. Wang, Cylindrical rotating triboelectric nanogenerator, *ACS Nano* 7 (2013) 6361–6366, <https://doi.org/10.1021/nn402491y>.
- M.H. Yeh, H.Y. Guo, L. Lin, Z. Wen, Z.L. Li, C.G. Hu, Z.L. Wang, Rolling friction enhanced free-standing triboelectric nanogenerators and their applications in self-powered electrochemical recovery systems, *Adv. Funct. Mater.* 26 (2016) 1054–1062, <https://doi.org/10.1002/adfm.201504396>.
- H.M. Yang, W.L. Liu, Y. Xi, M.H. Lai, H.Y. Guo, G.L. Liu, M.F. Wang, T. Li, X. Ji, X. G. Li, Rolling friction contact-separation mode hybrid triboelectric nanogenerator for mechanical energy harvesting and self-powered multifunctional sensors, *Nano Energy* 47 (2018) 539–546, <https://doi.org/10.1016/j.nanoen.2018.03.028>.
- D.J. Lacks, T. Shinbrot, Long-standing and unresolved issues in triboelectric charging, *Nat. Rev. Chem.* 3 (2019) 465–476, <https://doi.org/10.1038/s41570-019-0115-1>.
- G.Q. Xu, D. Guan, X. Yin, J.J. Fu, J. Wang, Y.L. Zi, A coplanar-electrode direct-current triboelectric nanogenerator with facile fabrication and stable output, *EcoMat* 2 (2020), e12037, <https://doi.org/10.1002/eom2.12037>.



**Yikui Gao** received his B. S. degree in Theoretical physics from Chongqing University. Currently, he is a master degree candidate in condensed state physics from Guangxi University. His current research interest is triboelectric nanogenerator.



**Xing Yin** received his master degree from Southwestern Institute of Physics in 2013. He received a Ph.D. in Beijing Institute of Nano energy and Nano systems, Chinese Academy of Sciences. His current research is Generation IV nuclear material



**Di Liu** received his B. S. degree in Material Science and Engineering from Nanjing University of Aeronautics and Astronautics. Now he is a Ph.D. candidate in Beijing Institute of Nanoenergy and Nanosystems, Chinese Academy of Sciences, China. His current research interest is triboelectric nanogenerators for energy harvesting and self-powered systems.



**Shengyang Chen** received his B. S. degree in Applied Physics from Jimei University. Currently, he is a master degree candidate in condensed state physics from Guangxi University. His current research interest is triboelectric nanogenerator.



**Linglin Zhou** received her Ph.D. degree from University of Science and Technology of China in 2018. Now she is a research assistant in Beijing Institute of Nanoenergy and Nanosystems, Chinese Academy of Sciences, China. Her current research focuses on the improvement of triboelectric nanogenerators and their applications in environmental pollutants treatment.



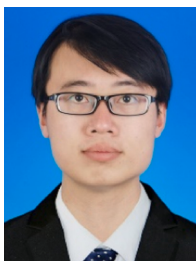
**Dr. Jie Wang** received his Ph.D. degree from Xi'an Jiaotong University in 2008. He is currently a professor at Beijing Institute of Nanoenergy and Nanosystems, Chinese Academy of Sciences. His current research interests focus on the energy materials, supercapacitors, nanogenerators and self-powered system.



**Shaoxin Li** received his B. S. degree in Composite Material and Engineering from Jiangsu University. Now she is a Ph.D. candidate in Beijing Institute of Nanoenergy and Nanosystems, Chinese Academy of Sciences, China. Her current research interest is triboelectric nanogenerators for sensor and self-powered systems.



**Zhong Lin (ZL) Wang** received his Ph.D. from Arizona State University in physics. He now is the Hightower Chair in Materials Science and Engineering, Regents' Professor, Engineering Distinguished Professor and Director, Center for Nanostructure Characterization, at Georgia Tech. Dr. Wang has made original and innovative contributions to the synthesis, discovery, characterization and understanding of fundamental physical properties of oxide nanobelts and nanowires, as well as applications of nanowires in energy sciences, electronics, optoelectronics and biological science. His discovery and breakthroughs in developing nanogenerators established the principle and technological road map for harvesting mechanical energy from environment and biological systems for powering a personal electronics. His research on self-powered nanosystems has inspired the worldwide effort in academia and industry for studying energy for micro-nano-systems, which is now a distinct disciplinary in energy research and future sensor networks. He coined and pioneered the field of piezotronics and piezo-phototronics by introducing piezoelectric potential gated charge transport process in fabricating new electronic and optoelectronic devices. Details can be found at: <http://www.nanoscience.gatech.edu>.



**Zhihao Zhao** received the Ph.D. degree in Materials Science and Engineering from Tianjin University in 2018. After graduation, he worked as a postdoctoral research fellow in School of Materials of Sun Yat-sen University. Currently, he is a visiting scholar of Beijing Institute of Nanoenergy and Nanosystems. His current research interests focus on dielectric/piezoelectric materials and triboelectric nanogenerators.